Imaging of terahertz surface plasmon waves excited on a gold surface by a focused beam

Raimund Mueckstein* and Oleg Mitrofanov

Department of Electronic & Electrical Engineering, University College London, Torrington Place, London, WC1E 7JE, UK
*raimund.mueckstein.09@ucl.ac.uk

Abstract: Surface plasmon polariton (SPP) waves formed near a tightly focused THz beam on a metallic surface are detected by an integrated sub-wavelength aperture THz near-field probe. The probe allows mapping the electric field pattern of the SPP wave and tracking the SPP propagation from the center of the focal spot. The SPP nature of the observed wave is confirmed by time-resolved measurements. Analysis of the detected patterns leads to an explanation of how THz SPP waves can be detected by the integrated sub-wavelength aperture probe.

©2011 Optical Society of America

OCIS codes: (240.6680) Surface plasmons; (110.6795) Terahertz imaging; (180.4243) Near-field microscopy; (320.7100) Ultrafast measurements.

References and links

1. A. V. Zayats, I. I. Smolyaninov, and A. A. Maradudin, "Nano-optics of surface plasmon polaritons," Phys. Rep. **408**(3-4), 131–314 (2005).
2. S. Kawata, *Near-Field Optics and Surface Plasmon Polaritons*, Topics in Applied Physics, Vol. 81 (Springer, Berlin, 2001).
3. A. Bouhelier, F. Ignatovich, A. Bruyant, C. Huang, G. Colas des Francs, J.-C. Weeber, A. Dereux, G. P. Wiederrecht, and L. Novotny, "Surface plasmon interference excited by tightly focused laser beams," Opt. Lett. **32**(17), 2535–2537 (2007).
4. H. Ditlbacher, J. R. Krenn, N. Felidj, B. Lamprecht, G. Schider, M. Salerno, A. Leitner, and F. R. Aussenegg, "Fluorescence imaging of surface plasmon fields," Appl. Phys. Lett. **80**(3), 404–406 (2002).
5. B. Hecht, H. Bielefeldt, L. Novotny, Y. Inouye, and D. W. Pohl, "Local Excitation, scattering, and interference of surface plasmons," Phys. Rev. Lett. **77**(9), 1889–1892 (1996).
6. E. Devaux, T. W. Ebbesen, J.-C. Weeber, and A. Dereux, "Launching and decoupling surface plasmons via micro-gratings," Appl. Phys. Lett. **83**(24), 4936–4938 (2003).
7. A. Kubo, N. Pontius, and H. Petek, "Femtosecond microscopy of surface plasmon polariton wave packet evolution at the silver/vacuum interface," Nano Lett. **7**(2), 470–475 (2007).
8. S. A. Maier, *Plasmonics: Fundamentals and Applications* (Springer, Berlin, 2007).
9. J. R. Knab, A. J. L. Adam, M. Nagel, E. Shaner, M. A. Seo, D. S. Kim, and P. C. M. Planken, "Terahertz near-field vectorial imaging of subwavelength apertures and aperture arrays," Opt. Express **17**(17), 15072–15086 (2009).
10. M. A. Seo, A. J. L. Adam, J. H. Kang, J. W. Lee, S. C. Jeoung, Q. H. Park, P. C. M. Planken, and D. S. Kim, "Fourier-transform terahertz near-field imaging of one-dimensional slit arrays: mapping of electric-field-, magnetic-field-, and Poynting vectors," Opt. Express **15**(19), 11781–11789 (2007).
11. K. Wang, and D. M. Mittleman, "Metal wires for terahertz wave guiding," Nature **432**(7015), 376–379 (2004).
12. H. Zhan, R. Mendis, and D. M. Mittleman, "Superfocusing terahertz waves below λ/250 using plasmonic parallel-plate waveguides," Opt. Express **18**(9), 9643–9650 (2010).
13. M. Gong, T. I. Jeon, and D. Grischkowsky, "THz surface wave collapse on coated metal surfaces," Opt. Express **17**(19), 17088–17101 (2009).
14. A. Bitzer, and M. Walther, "Terahertz near-field imaging of metallic subwavelength holes and hole arrays," Appl. Phys. Lett. **92**(23), 231101 (2008).
15. J. Saxler, J. G. Rivas, C. Janke, H. P. M. Pellemans, P. H. Bolivar, and H. Kurz, "Time-domain measurements of surface plasmon polaritons in the Terahertz frequency range," Phys. Rev. B **69**, 155427 (2004).
16. A. J. Huber, F. Keilmann, J. Wittborn, J. Aizpurua, and R. Hillenbrand, "Terahertz near-field nanoscopy of mobile carriers in single semiconductor nanodevices," Nano Lett. **8**(11), 3766–3770 (2008).
17. H. Kano, S. Mizuguchi, and S. Kawata, "Excitation of surface-plasmon polaritons by a focused laser beam," J. Opt. Soc. Am. B **15**(4), 1381–1386 (1998).
18. O. Mitrofanov, M. Lee, J. W. P. Hsu, I. Brener, R. Harel, J. F. Federici, J. D. Wynn, L. N. Pfeiffer, and K. W. West, "Collection-mode near-field imaging with 0.5-THz pulses," IEEE J. Sel. Top. Quantum Electron. **7**(4), 600–607 (2001).

19. O. Mitrofanov, I. Brener, M. C. Wanke, R. R. Ruel, J. D. Wynn, A. J. Bruce, and J. Federici, "Near-field microscope probe for far infrared time domain measurements," Appl. Phys. Lett. **77**(4), 591–593 (2000).
20. O. Mitrofanov, T. Tan, P. R. Mark, B. Bowden, and J. A. Harrington, "Waveguide mode imaging and dispersion analysis with terahertz near–field microscopy," Appl. Phys. Lett. **94**(17), 171104 (2009).
21. L. Novotny, and B. Hecht, *Principles of Nano-Optics* (Cambridge University Press, 2006).
22. Y. Cai, I. Brener, J. Lopata, J. Wynn, L. Pfeiffer, and J. Federici, "Design and performance of singular electric field terahertz photoconducting antennas," Appl. Phys. Lett. **71**(15), 2076–2078 (1997).

1. Introduction

Detection of surface plasmon polaritons (SPPs), the electro-magnetic waves confined to metallic surfaces, often presents experimental challenges [1,2]. In the optical domain several imaging methods have been developed to study SPP phenomena [2–7]. In the THz range, in contrast, imaging methods are not as versatile and only a few examples of SPP mapping have been reported: surface waves propagating along metallic wires, waveguides, and metallic surfaces have been detected by near-field electro-optic probes, photoconductive antennas, and scattering probes [8–15]. SPPs in the THz range are technologically important because they provide a possibility to develop subwavelength-size devices and offer the only opportunity to investigate nanoscale systems at THz frequencies [16]. Comprehensive imaging methods are essential to support SPPs investigations.

In this study we demonstrate the possibility of time-resolved high spatial resolution imaging of THz SPP waves by using an integrated sub-wavelength aperture THz near-field probe. The integrated design of the probe makes it sensitive to a SPP wave excited directly on its metallic surface. Taking advantage of this property we mapped the SPP wave near a THz beam focused on a metallic surface, a phenomenon that has not been observed at THz frequencies. Using temporally resolved measurements, we are able to track the SPP wave propagation away from the beam focus. Analysis of the observed SPP patterns and comparison with theoretical considerations allows us to explain the mechanism of SPP coupling into the near-field probe and to correlate the detected signal to a spatial derivative of the electric field of the SPP wave.

The understanding of the SPP coupling mechanism is essential for image interpretation in near-field microscopy and it will allow application of this method to studies of plasmonic effects in THz antennas, waveguides, metamaterials, and SPP-based sensors. In addition, the ability to detect the electric field of the SPP wave, E^{SPP}, rather than the intensity, can improve an understanding of SPP phenomena by providing the amplitude and phase information, which is hard to obtain in the optical domain.

2. Experimental results

In the experiment, the SPP wave was excited by focusing a THz beam on the metallic surface of the probe. Any tightly-focused beam possesses a small longitudinal E_z component that can produce a SPP wave [17]. In the THz range, this excitation can be realized efficiently with a beam focused directly on the metallic surface due to very small mismatch between the SPP wavevector k_{spp} and the free space vector k_0. In contrast to most experimental methods at optical frequencies, this configuration does not require the evanescent field coupling of the SPP waves between two media [17]; instead, the SPP wave is formed directly on the metal/air interface by the localized longitudinal E_z component of the incident field.

To detect the SPP wave we use an integrated sub-wavelength aperture near-field probe. It has a flat gold surface (thickness = 600 nm) with a small square-shape aperture (edge length a = 20 μm) and a photoconductive antenna located ~5 μm behind the aperture (Fig. 1(a)). Details of this probe design and its fabrication can be found in Ref. 18 and 19. THz pulses with a center frequency of 2 THz are generated in a ZnTe crystal by optical rectification of 100 fs pulses from a Ti:sapphire laser. The THz beam is coupled into a hollow dielectric-lined cylindrical metallic waveguide in which it propagates as the linearly polarized HE_{11} mode [20]. At the waveguide output end, a high-NA hyperhemispherical Si lens (radius = 1 mm) focuses the THz beam on the metallic surface of the near-field probe (Fig. 1(a)). The probe is gated by the Ti:sapphire laser pulses as in a standard THz time domain spectroscopy setup and

is oriented to detect the x-polarized THz field component [18]. The average laser power for THz pulse generation was 200 mW and 5 mW for gating the detector antenna. Time-domain waveforms are sampled with the interval of 67 fs using an optical delay stage. To map the SPP waves, computer-controlled translation stages raster-scan the lens-waveguide assembly with respect to the probe.
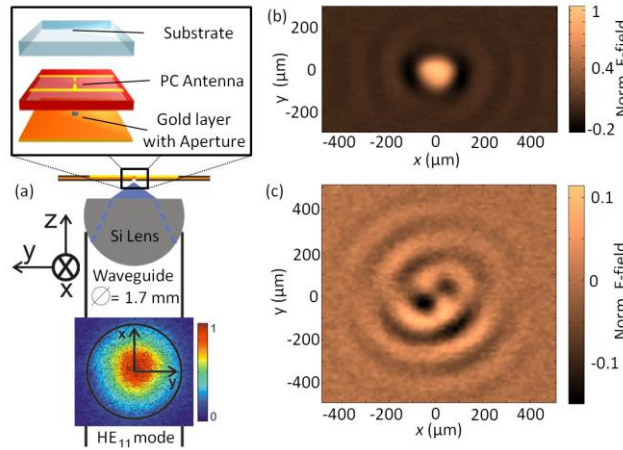

Fig. 1. (a) Schematic diagram of the experimental setup with all the elements of the integrated sub-wavelength aperture probe shown in a magnifying box. The inset at the bottom shows the E-field of the THz beam at the waveguide output. Electric field patterns detected near the beam focus for two cases: the THz beam is polarized parallel (b) and perpendicular (c) to the detector antenna. The electric field values in (b) and (c) are normalized to the maximum value in (b).

A map of the instantaneous electric field detected by the aperture probe in the region of the focused x-polarized THz beam is shown in Fig. 1(b). The probe is positioned in the focal plane, at a distance of $z = 40$ μm away from the flat surface of the Si lens. The image shows a moment in time, t_0, corresponding to the peak of the incident THz pulse. The focal spot is visible in the center of the image as a bright area. In addition, concentric fringes that extend in the x-direction are present around the focal spot. As it will be shown later, these fringes correspond to the SPP wave emanating from the focal area. The SPP fringes can be seen more clearly in Fig. 1(c), which shows the detected field distribution for the incident THz beam polarized in the y-direction. The image shows fringes in a shape of a spiral pattern. Since the incident field is orthogonally polarized with respect to the antenna, the incident field is not detected and the fringes cannot be caused by diffraction of the incident wave.

The origin of the fringes is determined with help of time-domain data obtained by delaying the optical probing pulses that gate the antenna detector. In this experiment, the waveguide-lens assembly was scanned along a line either in the x- or y-direction while the time-domain waveform of the THz pulse was recorded (Fig. 2(a)). The detected field is presented as a space-time map in Fig. 2(b). In the center of the map the focused beam can be identified as a series of short bright horizontal lines corresponding to the wave crests of the incident THz pulse. Away from the center, the horizontal lines turn into a series of straight tilted stripes arranged symmetrically in a Λ-shape pattern. The slopes of these stripes indicate that this wave propagates away from the focal spot along the metallic surface with a speed close to the speed of light, $v_{exp} = (3.0 \pm 0.1) \cdot 10^8$ m/s. The only wave that can propagate along the metallic surface is the SPP wave. Considering a horizontal section of the space-time map shown by a dashed line at $t = t_0$ in Fig. 2(b), it becomes clear that this SPP wave appears as a series of fringes in the instantaneous xy-plane images as seen in Fig. 1(b).

The strongest SPP wave is expected to form when the beam is focused to the minimal size and the longitudinal E_z component of the beam that produces the SPP wave is maximal. To determine the focal plane location, the space-time maps were recorded for various positions of the probe with respect to the lens, z (Fig. 2(c)). For positions $z = 200$ μm and 100 μm, both in

the *xt*- and in the *yt*-maps, one can see a wide spherically diverging wavefront, which corresponds to the focused incident THz beam. For *z*-distances approaching the lens surface, the spherically diverging wave is replaced by the Λ-shape pattern of the SPP wave. Note that the SPP stripes only appear in the *xt*-map, not in the *yt*-map. It is consistent with the fact that the SPP wave formed by the focused beam does not propagate in the direction perpendicular to the incident field polarization [3,17]. The series of space-time maps in Fig. 2(c) determines that the focal plane is located at *z* = 40 μm and confirms that the SPP wave is generated most efficiently when the metallic surface coincides with the focal plane.
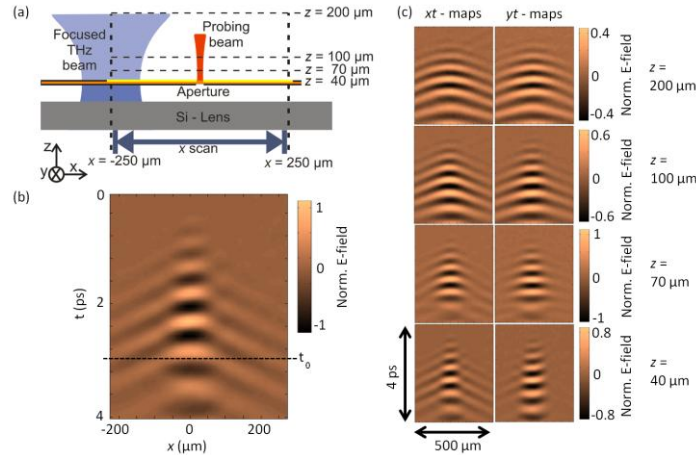

Fig. 2. (a) Schematic diagram of the experimental setup, where all the elements are drawn to scale. The shape of the incident THz beam is obtained by measuring the FWHM at the respective *z*-positions. (b) The normalized *xt*-map of the detected field for the aperture-lens distance *z* of 40 μm. The space-time maps in (c) show the measured electric field along the *x*- and *y*-axis respectively for different positions of the metallic surface with respect to the lens. Data in all maps (c) are normalized to the maximum value in the *xt*-map for *z* = 70μm.

The SPP wave can also be distinguished from the incident THz beam in Fig. 2(b) by analysis of the electric field amplitude. Figure 3(a) shows the normalized amplitudes as a function of distance from the focused THz beam center in the *x*- and *y*-directions for a probe-lens separation of *z* = 40 μm. The electric field values were taken along the ridge of one of the wave crests, as depicted by the dashed line in Fig. 3(b). Since the SPP wave does not propagate along the *y*-axis, the electric field values along a similar trace were taken to show the amplitude decay in the *y*-direction. One can see that for distances close to the center ($0 < x < 80$ μm), the decays in both the *x*- and *y*-direction follow a Gaussian shape, which is characteristic of the incident THz beam. However, beginning from a certain point ($x \sim 100$ μm), an additional component is present along the *x*-axis. This component can be described by a cylindrically diverging SPP wave according to [3,5] (for $x > 0$):

$$E^{SPP}(x, y = 0) = \frac{1}{\sqrt{|x - x_0|}} \cdot e^{-\frac{|x - x_0|}{2 \cdot L_{SPP}}}. \tag{1}$$

The center of the cylindrical SPP wave at $x_0 = 45$ μm corresponds to the maximum value of the E_z component within the focused THz spot [21]. The SPP decay length L_{spp} was estimated to be 200 ± 100 μm, which is smaller than the expected theoretical decay length of several millimeters [2,8,21]. The reduced decay length is likely due to the presence of the Si lens, which confines the electromagnetic energy much closer to the metallic surface and hence increases absorption. This analysis of the electric field amplitude decay in the *x*- and *y*-directions confirms that the observed wave pattern is a superposition of a Gaussian beam, which corresponds to the incident THz field, and a cylindrically divergent SPP wave.
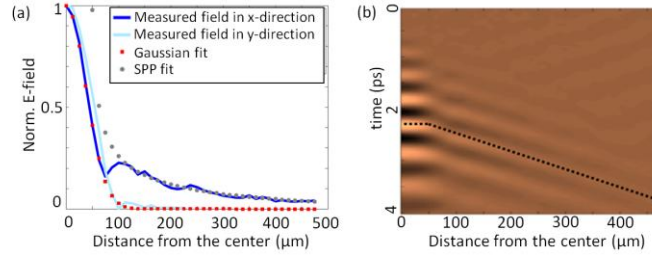
Fig. 3. (a) Normalized detected electric field amplitude along the *x*- and *y*-axis as a function of distance from the optical axis. To track the SPP wave amplitude, the electric field values are taken along a trace marked in the *xt*-map (b) with a dotted line. A Gaussian fit and a SPP fit according to Eq. (1) are added to the plot (a) for comparison.

3. SPP coupling into the probe

Although the fringes in Fig. 1(b, c) are undoubtedly caused by the SPP wave, the question of how the SPP wave couples into the aperture of the probe has not been addressed yet. To explain the coupling mechanism, it is useful to consider the theoretical SPP field distribution caused by the focused THz beam on a continuous metallic surface and compare it to the experimental observations. A linearly polarized focused beam has two peaks of the longitudinal field, E_z, close to the opposite edges of the focal spot [3,17,21]. These two peaks are located along the axis parallel to the direction of polarization and are inherently 180° out of phase. If the beam is focused on a metallic surface, these peaks induce a non-equilibrium localized surface charge, which generates the SPP wave. For simplicity, the peaks in the E_z distribution can be considered as two point-like SPP "sources", and the overall SPP wave as the superposition of the two corresponding waves. The electric field and the surface charge of the SPP wave are schematically illustrated in Fig. 4(a).

A small aperture on the surface locally obstructs the natural SPP wave propagation and causes discontinuities in the surface charge distribution σ at the aperture edges. This discontinuity in σ creates a potential difference at the opposite aperture edges. Since the charge distribution follows the SPP wave pattern (E^{SPP} and σ are related by the surface boundary condition), the potential difference corresponds directly to the difference in E^{SPP} at the opposite aperture edges. The potential difference also implies that there is a tangential field component over the aperture. This tangential field couples through the aperture and induces a current in the photoconductive antenna located in the near-field zone of the aperture (Fig. 4(b)). The detected antenna current i_A therefore is directly related to the difference in the normal component of E^{SPP} at the positions of the aperture edges.

The detector antenna in this work is sensitive mainly to the *x*-component of the tangential field. As a consequence, the detected current i_A in the *xy*-plane can be related to E^{SPP} by a simple expression for the aperture edge length $a \ll \lambda_{SPP}$:

$$i_A \propto E^{SPP}(x, y)\bigg|_{x+\frac{a}{2}} - E^{SPP}(x, y)\bigg|_{x-\frac{a}{2}} \approx \frac{d}{dx} E^{SPP}(x, y) \cdot a. \qquad (2)$$

It is important to note that the integrated aperture probe detects the derivative of $E^{SPP}(x, y)$ with respect to the *x*-coordinate, rather than $E^{SPP}(x, y)$ itself. This result is schematically illustrated in Fig. 4(a, b), where the original anti-symmetric E^{SPP} distribution (a) changes into a symmetric pattern detected by the probe (b).

The relationship between i_A and E^{SPP} described in Eq. (2) is also verified by comparing the detected SPP wave images (Fig. 1(b, c)) with expected patterns. The E^{SPP} distribution formed by the focused beam was calculated using the localized SPP source model discussed earlier. The simulated i_A pattern in the case of the incident THz beam polarized in the *x*-direction shown in Fig. 4(c) closely resembles the detected pattern in Fig. 1(b). Only the central area near the focal point is different because the experimental image also contains a superimposed

contribution from the *x*-polarized incident THz beam. Note that the *odd* symmetry of the actual SPP pattern, $E^{SPP}(x) = -E^{SPP}(-x)$ (which follows the symmetry of E_z shown in the inset of Fig. 4(c)) is changed in the expected image: $i_A(x) = i_A(-x)$ due to the differential relation between E^{SPP} and i_A, according to Eq. (2).

It is useful to consider the case of the *y*-polarized incident field, in which the SPP pattern has the *even* symmetry: $E^{SPP}(x) = E^{SPP}(-x)$. The expected image is now *odd* with respect to the *x*-coordinate: $i_A(x) = -i_A(-x)$. Since Eq. (2) does not change the *y*-coordinate symmetry, the *odd* symmetry of the SPP wave with respect to the *y*-coordinate, $E^{SPP}(y) = -E^{SPP}(-y)$, is conserved in the expected pattern. As a result, the overall i_A pattern in Fig. 4(d) exhibits the *odd* symmetry for both coordinates: $i_A(x,y) = -i_A(-x,y)$ and $i_A(x,y) = -i_A(x,-y)$, similar to the experimentally detected spiral pattern in Fig. 1(c).

We note that the map in Fig. 1(c) shows a weak SPP wave propagating along the *y*-axis (*x* = 0). In theory, however, there should be no potential difference on the right and the left side of the aperture positioned along this axis. The experimentally detected field is likely to be due to the offset design of the antenna dipoles, which causes a non-zero sensitivity of the detector antenna to the *y*-polarized electric field [22]. In this study, the antenna response to the *y*-polarized field is experimentally estimated to be ~30% of the response to the *x*-polarized field. We also note that SPP maps similar to Fig. 1(b) and Fig. 2(b) were measured with another probe, which contains a 50μm aperture.

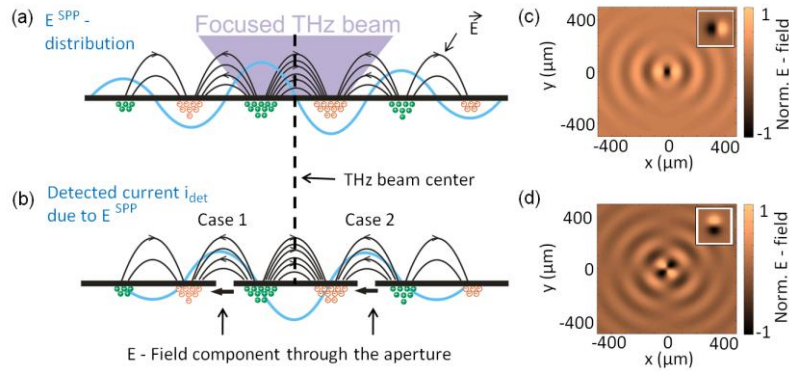Fig. 4. Coupling of the SPP wave into the aperture. (a) E^{SPP} (blue line) and the corresponding charge density distribution σ of the SPP wave caused by the focused THz beam. (b) Detected current i_A (blue line) due to E^{SPP}. The horizontal arrows show the electric field coupled through the aperture at two points −*x* (case 1) and + *x* (case 2). (c) Simulated distribution $i_A(x,y)$ according to Eq. (2) for the *x*- polarized and the *y*- polarized (d) incident THz beams. The insets in (c) and (d) show the corresponding E_z field in the beam focus.

4. Conclusions

This work demonstrates that the integrated sub-wavelength aperture probe allows mapping THz SPP waves, despite the fact that the electric field of the SPP wave is normal to the metallic surface of the probe. The theoretical considerations and the experimental results presented above prove that the integrated sub-wavelength aperture probe detects the derivative of $E^{SPP}(x,y)$ with respect to the spatial coordinate representing the detector antenna orientation. We support this finding by explaining the coupling mechanism and by imaging a previously unnoticed effect, a SPP wave excited by a focused THz beam on the metallic surface. The understanding of the SPP coupling mechanism is essential for image interpretation in THz near-field microscopy.

Acknowledgments